Final Master Project

Universidad Zaragoza

In-situ electron microscopy studies of carbon nanomaterials

David Sebastián Valenzuela

Tutor : Raúl Arenal

Academic year 2018/2019

LMA
LABORATORIO
DE MICROSCOPIAS
AVANZADAS

Facultad de Ciencias
Universidad Zaragoza

Instituto Universitario de Investigación
en Nanociencia de Aragón
Universidad Zaragoza

TABLE OF CONTENTS

1 Abstract

High resolution transmission electron microscopy (HRTEM) imaging and electron energy loss spectroscopy (EELS), when conducted in a TEM, are very powerful techniques for studying the structure and composition of nanomaterials at the local scale. Their impact and richness can even been improved if, in parallel, the response of the nanomaterials to an external stimuli is investigated (in situ conditions). During this Final Master Project, these techniques, under in situ conditions, have been developed to investigate two different kind of carbon-based nanomaterials: endohedral functionalized single-walled carbon nanotubes (SW-CNTs) with fullerenes (peapods) and graphene oxide (GO).

Electron irradiation in-situ TEM experiments have been carried out on these peapods systems. The evolution of this carbon hybrid nanostructure under electron irradiation has been studied. Experimental results showed that, through the energy applied by electronic irradiation, vacancies were formed in the wall of the nanotube resulting in the reaction with the fullerene and finally forming a nanobud (combination of a SWNT and spherical fullerene).

The second system that we have investigated was graphene oxide. We have studied the electrical characteristics and the evolution of the structure and composition of graphene oxide via in situ electrical TEM measurements. To prepare the sample, a dual beam microscope has been employed to deposit the GO flake on a TEM nano-chip. Then, we proceeded with the application of in situ electrical measurements to observe the changes in the GO by taking low loss and core loss EEL spectra. These spectra allow us to study the composition, thickness and sp^2 / sp^3 of the sample. We have measured the electrical conductivity of GO and the relationship with the reduction and graphizitation of a GO flake.

All these in situ TEM works have provided important inputs for the knowledge of these particular carbon nanostructures, their transformation and their properties. Some of these results will have a clear impact on the application of these nanomaterials.

2   Introduction

The last three decades, special attention has been paid to carbon-based nanomaterials due to their unique physical & chemical properties [1,2]. Indeed, a significant interest has been devoted to some of the different carbon nanostructures as fullerenes, nanotubes, graphene and nanodiamonds [3]. These nanomaterials have very interesting mechanical, electrical, optical properties, which have opened the door for some applications in different technological fields: electronics, energy, medicine...[2,4,5,6] In these works, we focused on the study of three of such carbon nanostructures: fullerenes, nanotubes and graphene (in particular graphene oxide).

Since the seminal works of S. Iijima on carbon nanotubes (NTs) in 1991 [7], their structure, properties and applications carbon nanotubes have been deeply investigated [8]. It is also interesting to note that the surface of a nanotube governs its chemical properties, offering the possibility of encapsulating or grafting molecules for modifying and improving the opto-electronic properties of the NTs [9,10]. In this sense, one of the most attracting systems is the encapsulation or filling of NTs with fullerenes [11,12,13]. This hybrid system is known as "peapods" due to their final morphology. This new resulting hybrid material offers a fascinating playground with interesting possibilities of tuning its optoelectronic and mechanical properties [14]. In fact, as we will see in this report, it is possible to modify completely the original structure of such nanomaterials via, for instance, electron irradiation and then obtaining new nanostructures showing new functionalities and applications.

Graphene is another allotropic form of carbon. Due to its interesting properties and promising applications, graphene has been widely investigated this last decade [2,4]. One closely related material to graphene is graphene oxide (GO). Indeed, GO is a form of heavily oxygenated graphene layers having a significant amount of functional groups on their basal planes (as the epoxy and hydroxyl groups) and at the edges of the sheets (as carbonyl and carboxyl groups). Thus, this material consists in a mixture of sp^2 and sp^3 carbons, in presence of a large number of defects and physisorbed as well as chemisorbed water in these flakes. This structural and chemical complexity is due to the presence of these oxygenated functional groups (OFGs). However, this complex material offers very interesting possibilities of tuning via its reduction (production of reduced GO (rGO)). This rGO, once the reduction and graphitization of GO are fully achieved, can be very close to perfect graphene. This reduction can be performed following thermal or chemical ways, but in both cases, it is very important to monitor the number/density and distribution of the OFGs in the GO structure for controlling this reduction process [15,16]. Indeed, this process remains a fundamental and critical open question, which

has a significant importance on the physical and chemical properties of this material and its reduced derivative.

In-situ transmission electron microscopy (TEM) is a very appropriate approach for investigating, at the local scale (sub-nanometer, even atomic level), the behavior the nanomaterials under external stimuli (heating, cooling, electrical biasing, strain…) and in parallel getting information about the atomic structure and configuration [17,18]. In addition, electron irradiation, when performed in a TEM, allows to modify the matter under mastered conditions (i.e. controlling the electron dose) offering the possibility to produce new nanostructures [19]. Both in-situ TEM approaches (study the response of the nanomaterials to external stimuli and matter's transformations) allow very interesting studies and open the door for new applications of nanomaterials.

In these works, we have developed in-situ TEM studies on the two different systems described above: peapods and GO. In the former of these systems, we have investigated the transformation of the peapods via electron irradiation. We have observed the combination of a fullerene and the end of a nanotube to form a nanobud (combination of a CNT and a spheroidal fullerene) [20]. This is an interesting result as we shed light on the formation of these nanostructures. In addition, we have investigated, via in-situ electrical TEM experiments, the electric resistance behavior of graphene oxide. We have studied how GO's reduction and graphitization affect its electric properties. These works are important for understanding the GO transformation and its properties, which is crucial for its potential applications.

For carrying on such studies, we have developed these in-situ TEM studies in combination with high-resolution TEM imaging and electron energy loss spectroscopy (EELS) measurements. These TEM techniques are the most appropriated ones for extracting important structural and chemical information relevant for the material behavior during the in-situ transformations.

3 Techniques

3.1 Transmission electron microscopy (TEM)

Transmission electron microscopy (TEM) is one of the most powerful tools for the study of nanomaterials as it is possible to get the structural and chemical information of the nanostructures at the atomic level [18,19]. In a TEM, a beam of accelerated electrons, with common energies between 40-400 keV, is transmitted through a specimen to form an image, a diffraction pattern or to obtain a spectrum. The specimen is an ultrathin section less than 100 nm thick or a suspension deposited on a grid (usually on a carbon membrane). Figure 1 displays a schematic representation of a TEM. This instrument contains four parts: electron source,

illumination system, sample holder, and imaging system. The electron beam is formed by condensing and accelerating the electrons extracted from a sharp refractory metal tip (tungsten filament or a lanthanum hexaboride crystal) which emits electrons when being heated or via field emission process. After leaving the electron source, there is the illumination system, which is formed by a series of electromagnetic lenses and metal apertures for condensing the electron beam. This illumination system only allows electrons within a small energy range to pass through, so the electrons in the electron beam will have a well-defined energy. The specimen, which is located in the sample holder (placed at the center of the polepiece of the objective lens) is illuminated by the electron beam and there is now the role of the image system. In this system, this objective lens is the first-stage (and the most important) lens to form an image using electrons exiting from the sample. The importance of this objective lens is because the performance of this lens determines the quality of the image (resolution, contrast, etc). The formed image is then enlarged by the intermediate lenses and finally projected by projector lenses on a phosphorescent screen or a CCD camera. Apertures may be inserted along the optical axis at the level of the objective focal plane (objective aperture) or image plane (selected area aperture), Fig. 1. The first one allows selecting particular spots of the diffraction pattern deriving from the illuminated specimen (Bragg diffraction) in order to restrict the contribution to image formation to only specific families of crystal planes. The selected area aperture is used to choose the area of the specimen whose diffraction pattern is projected on the fluorescent screen (diffraction mode of TEM microscope), see Fig. 1(b).
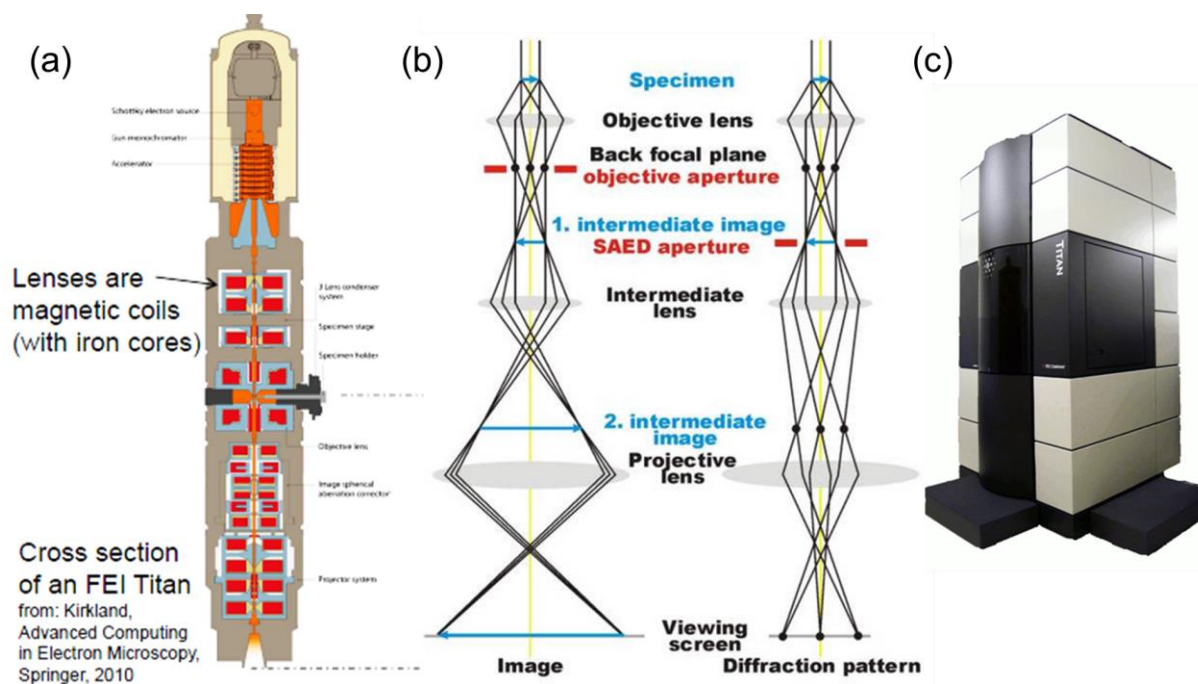

Figure 1. (a) Schematic representation of an aberration corrected TEM microscope. (b) Two operative modes (imaging on the left) and diffraction (on the right) of a TEM. (c) Photography of the aberration corrected TEM microscope used in this study (FEI Titan Cube 60-300 kV at the LMA-INA-U. Zaragoza facility).

The spatial resolution is defined as the shortest distance between two features in the specimen that appears distinct in the image and this spatial resolution is based in the Rayleigh criterion:

$$r = 0.61\lambda/n \sin\mu \tag{1}$$

where λ is the probe wavelength and $n \sin\mu$ the numerical aperture of the objective lens, with μ its semi-angle of collection. Typically, with an electron wavelength of 0.0037 nm (at 100 kV) and 10 mrad numeric aperture, the resolution is 0.22 nm.

These works have been conducted using the FEI Titan Cube 60-300kV, which is equipped with a Cs image corrector and a Gatan Tridiem spectrometer, see Fig. 1. We worked at low acceleration voltage (80 kV). Particular attention has been paid to avoid contamination during the acquisitions. Two different TEM techniques have been developed for performing these works: high resolution TEM (HRTEM) imaging and electron energy loss spectroscopy (EELS), see below.

3.1.1 High resolution TEM (HRTEM) imaging

HRTEM imaging mode provides access to the crystallographic structure, at the atomic scale, of a specimen. For this reason, this is an invaluable technique in materials science. It is worth to mention that carbon nanotubes were identified using this technique. Indeed, HRTEM remains the most widely employed technique for investigating both their morphology and structure [19,21].

TEM image contrast is due to the scattering of the incident beam by the specimen. In this sense, the electron wave can modify both its amplitude and its phase once is going through the sample and both kind of modifications provide image contrast [21]. Thus, in TEM we should distinguish between amplitude contrast and phase contrast. HRTEM is based in phase contrast. Indeed, a high resolution image depends on phase changes of the electron waves due to the specimen (scattering) and the electromagnetic lenses, especially the objective lens. It is worth mentioning that carbon nanotubes (which will be our system of study for HRTEM investigations, see below) can be considered as a weak phase object. Under this context, great simplifications can be made in the electron imaging theory (nonlinear imaging process and dynamical diffraction effects can be neglected to some extent), which makes easier the imaging interpretation [21].

In our case, we have combined in-situ TEM electron irradiation experiments within HRTEM imaging for investigating, at the atomic level, the peapods transformation.

3.1.2 Electron energy loss spectroscopy (EELS)

EELS is a spectroscopic technique that provides valuable information on materials and biological specimens complementary to the usual TEM techniques where the structure and morphology are investigated. EEL spectra contain information about valence/conduction electron density, electronic band structure, optical properties (studies on the low-losses energy region), chemical bonding and oxidation state (electron energy loss near-edge spectroscopy (ELNES)), elemental composition including quantification.

EELS measures the energy loss suffered by the incident electrons due to their interaction with the sample. The majority of primary fast electrons pass through the sample without undergoing any scattering event. These electrons reach the spectrometer conserving their initial energy and form the zero-loss peak (ZLP or elastic peak), at zero energy loss, which is the most intense feature of the spectrum, see Fig. 2. Two different regions can be distinguished: (1) low-losses (0-50 eV) and (2) core-losses (> 50 eV). The study of the low-losses provides direct access to the dielectric properties of a material because this region corresponds to the excitation of electronic states close to the Fermi level. The core-loss region corresponds to the analysis of absorption edges - the excitation in the material of an electronic transition from a core shell. These edges contain near edge fine structures (ELNES) with chemical information. Thus, EELS in the core loss region mainly provides chemical information of the specimen [17,22].
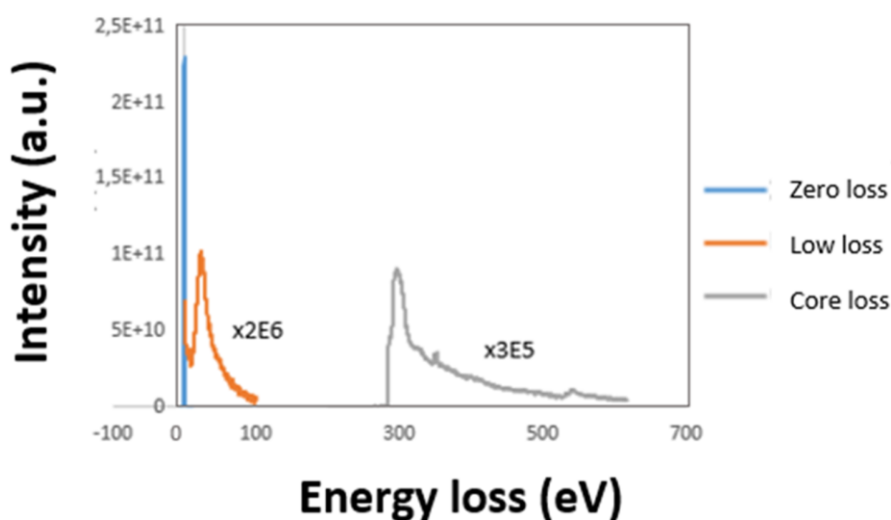

Figure 2. Global EELS spectrum acquired on a GO flake. Two regions can be distinguished: (1) low-losses (0-50 eV) and (2) core-losses (> 50 eV).

The EELS experiments have been performed in the FEI Titan Cube microscope, working at 80 kV in the TEM diffraction acquisition mode. The size of the analyzed area was around 200 nm. Convergence and collection angles were 6.3 and 19.7 mrad, respectively. Typical energy resolutions (full-width at half-maximum of the ZLP) of the measurements were better than 0.8 eV. We have used an energy dispersion of 0.2 eV/channel. The typical acquisition times for

core-loss and low-loss spectra were 0.5*50 s and $10^{-6}*50$, respectively. After collecting the data, each EEL spectrum has been calibrated. In the case of the core-loss spectra, the background has been subtracted by modeling the inverse power law function and for the low-loss spectra; the tail of ZLP has also been removed using a power law subtraction method. After performing these treatments, the spectra can be analyzed, see below.

In these works, different parameters regarding the GO materials have been obtained from the analysis of the EEL spectra in both, low-loss and core-loss, regions. These parameters are: the atomic content of oxygen/carbon, the presence (and behavior during the treatments) of the different OFGs (by ELNES analyses), the thickness and the sp^2/sp^3 ratio.

The **electrical in-situ treatments** have been performed employing a DENSsolutions Lightning TEM holder. This holder allows to perform electrical biasing and temperature-dependent in situ TEM measurements. The samples have been measured using specific chips for this holder, see Section 4. These chips are formed by Si_xN_y membranes.

3.2   Dual beam – focused ion beam (FIB)

A typical dual beam is formed by a scanning electron microscope (SEM) and a focus ion beam (FIB). This kind of instrument consists of a column of charged atoms (commonly Ga^+) used for imaging or for milling the sample, and a column of electrons (a scanning electron microscope (SEM)) for the observation and analysis of the specimen. The FIB can also be employed for ion welding of metal contacts on micro- and nano-scale devices [23,24].

For these studies, we have employed the FIB FEI Helios 650 working at 30 kV and a current of 7,7 pA. SEM images were acquired at different magnifications and currents.

Figure 3. Photography of the FIB FEI Helios 650 used for developing these works.

4 Materials

4.1 Carbon Nanotubes Filling with Fullerene - Peapods.

Carbon nanotubes (C-NTs) are one of the most representative structures in nanoscience and nanotechnology. Employing a heuristic model, the structure of a single-walled nanotube (SWNT) can be conceptually considered equivalent to a sheet of graphene rolled-up forming a tube [25]. The last 3 decades, the research activity on these nanostructures has been (and still is) very high. This interest is due to the fact that CNTs possess unique electrical, mechanical, optical, thermal properties [25]. For instance, CNTs show a very interesting combination of stiffness, strength, and tenacity as compared to other fiber materials, which usually lack one or more of these properties [25,26]. In addition, the electrical and thermal conductivities of CNTs are also very high and comparable to other conductive nanomaterials [25]. All these exceptional properties make C-NTs very good candidates for a broad range of applications, from electronic to energetic, medical and biological uses [26]. A carbon nanotube has nanometer scale in diameter but a length from um to cm. This great aspect ratio makes it a quasi-one-dimensional material. CNTs can be divided into two types based on the number of walls as single-walled (SWNTs) and multi-walled (MWNTs). MWCNTs generally have larger outer diameters (2.0 – 100 nm) than SWCNTs (0.4 – 8.5 nm) and consist of a varying number of concentric SWCNT layers, with an interlayer spacing of about 0.34 nm . There exist infinitely many geometrical ways to form a nanotube resulting in different diameters and microscopic structure of the tubes. For example, there are different ways of wrapping a graphene sheet into a cylindrical nanotube. The three basic ways are producing zig-zag, armchair or chiral configurations [25]. It is important to mention that the electronic properties of carbon nanotubes depend strongly on their microscopic structure. A small change in the may lead to two different types of conductivity (metallic and semiconducting) [26]. Under this context, in the introduction, it has been mentioned that a way to control their electronic properties can be via doping and a possible way will be the endohedral functionalization. In these works, we have developed such kind of functionalization via the filling of SWNTs with fullerenes.

Fullerenes are other kind of interesting carbon nanomaterials discovered in 1985 [28]. These molecules are formed by carbon atoms connected by single and double bonds. The most common fullerene is this one formed by 60 atoms (C_{60}), known as bucky-ball, because its structure is similar to this one of the standard soccer ball. Since the first fullerenes' synthesis, via laser vaporization methods, there has been a great interest in these molecules due to their physical and chemical properties and potential applications in electronic devices, imaging materials, magnetic recording and environmental processes. [28,29]

Nowadays, the interest in the functionalization of fullerenes is increasing since they are more soluble in certain solvents and could be interesting to make new materials. In 1993 it was synthetized $C_{60}H_2$ and from that moment other functionalized fullerenes have been produced. In our case, we have worked on fullerenes containing a chain with S atoms, $C_{59}N$-DT.

The bucky-ball (C_{60}) was the first molecule to be introduced in a carbon nanotube. This new hybrid structure was confirmed by HRTEM and was called peapod [28,29]. We have then worked on this kind of heterostructures based on peapods, but using $C_{59}N$-DT molecules for filling the SW-CNTs.

It is important to mention that SW-CNTs tend to form bundles. In order to carry out the debundling of CNT samples, which is needed for studying them and for their applications, a surfactant is commonly used to create a micelle in an aqueous medium, isolating the nanotubes previously separated by ultrasounds [30,31].
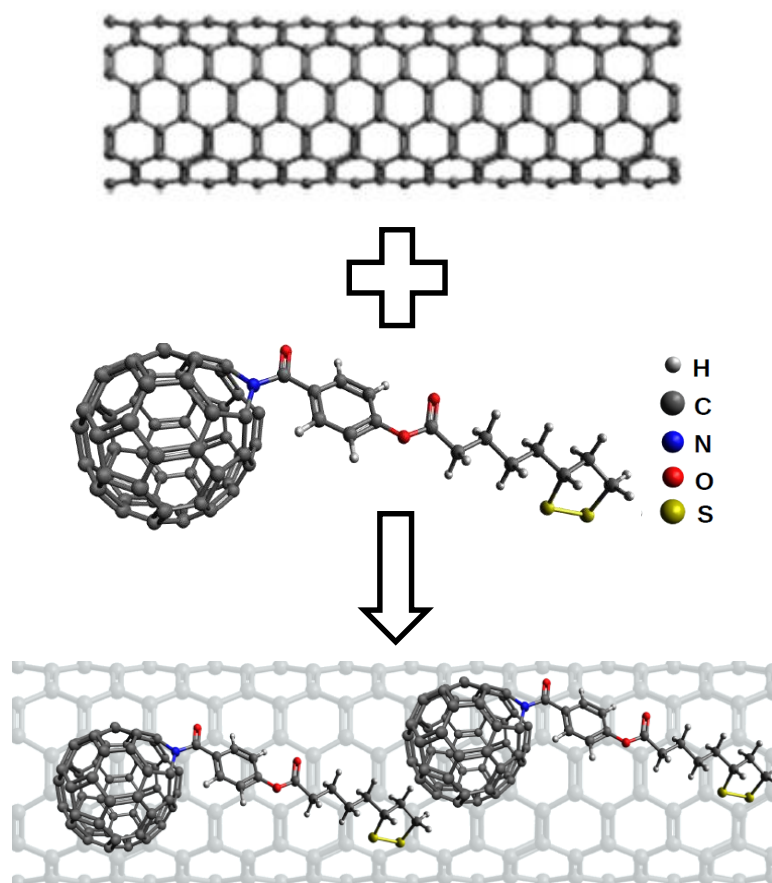

Figure 4. Schematic synthesis process of peapods formed by SW-CNTs and $C_{59}N$-DT fullerenes.

The peapods production has been developed using open ends carbon nanotubes and the $C_{59}N$-DT fullerenes from our collaborators from the team of Prof. Tagmatarchis (NHRF, Athens – Greece). The procedure for getting the peapods is the following one: First, SW-CNTs and

fullerenes were diluted in a toluene solution. For filling the NTs with the fullerenes, this solution was placed at 110 °C in an inert atmosphere for 24 hours. Then, the solution was filtered and cleaned to remove the fullerenes and other materials that were not inside the CNTs. The resulting powder was added to a solution of propanol which was centrifuged and re-dried to obtain the peapods. The last step was the TEM sample preparation. For getting a good TEM specimen, it is important to have a sample well dispersed and in a low concentration for avoiding NTs' agglomeration. Thus, a solution of ultrapure water with sodium cholate, which acts as a surfactant, was prepared, and this solution containing the peapods was ultrasonicated. Finally, we deposited a drop of this solution on holly carbon TEM grids.

4.2 Graphene oxide

The last decade, particular attention has been paid to graphene oxide (GO). This is due to its unique properties and its possible reduction to obtain reduced graphene oxide (RGO) having properties similar to those of the graphene.
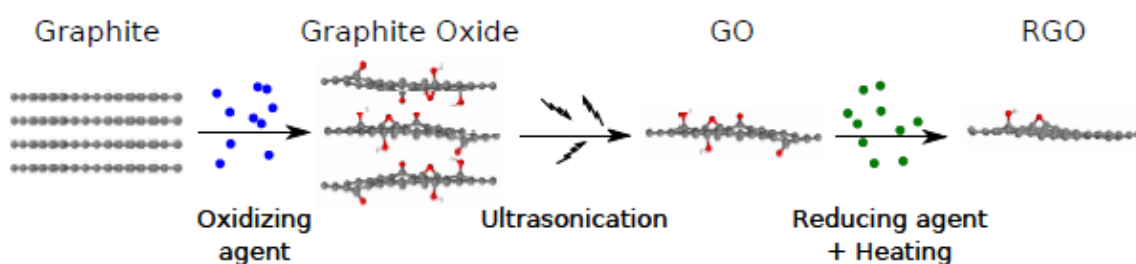

Figure 5. Schematic description of obtaining of GO and RGO from graphite [17]

GO is commonly obtained using the Hummers method. Graphite is treated with an oxidizing agent to oxidize the material, and then, by exfoliation of graphite layers obtain GO, as shown Figure 5. Next step, reduced GO (RGO) can be derived from GO using a reducing agent to remove the oxygen functional groups (OFGs) [17].

In 1859, B.C. Brodie was the first to investigate the structure of GO [27]. However, atom models were not realized until several years later. Nowadays, the model of Lerf and Klinowski is the most known (Figure 6). In this model, two types of OFGs are distinguished, those that are located at the edges of the sheet and those that are randomly distributed in the basal plane. The OFGs found on the edge correspond to carboxyl and carbonyl groups. However, those located in the basal plane correspond to the hydroxyl and epoxy groups [32].

It is also important to note that oxygenized areas, having a high amount of OFGs, contain high amounts of carbon domains showing sp^3 hybridization and then, this material has a significant insulating character. In fact, depending on the oxygen content, (reduced) GO-based materials undergo insulator-semiconductor-semimetal transitions with reduction [32].

Although GO comes from graphite (hydrophobic material), it is hydrophilic due to the presence of the OFGs that allow interaction with water by hydrogen bonds. However, this presence of functional groups does not break the 2D structure of the material. Indeed, in hydrated conditions, when assembled into a stacked layer structure, water remains trapped between the assembled GO layers. The amount of intercalated water defines the interlayer distance between the GO sheets, up to about 12 Å [33]. Low temperature thermal treatments (usually up to 100 ºC) can be used to reversibly control the hydration state but higher temperatures are required to remove the OFGs and restore the pathways with sp^2 character to convert the electrically non-conducting GO papers into conductive electrode materials. However, thermal treatments also lead to exothermic water-induced reactions (at Tres. < 120 ºC) that are responsible for irreversible damage in the GO. The water present in the GO layers can be **physisorbed water** (water in close contact to the surface of GO; this molecules can be easily and reversibly removed by low-temperature treatments) and **chemisorbed water** (water molecules linked to the OFGs by hydrogen bonds) [33,34].
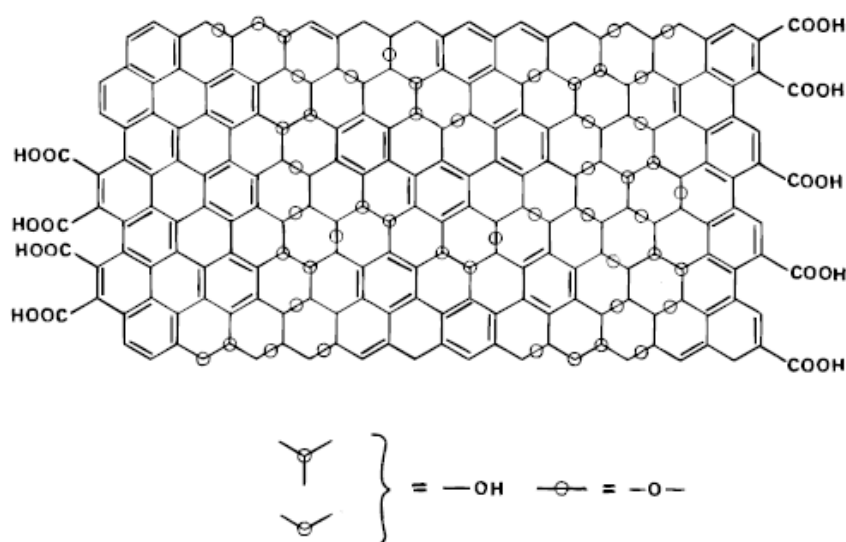

Figure 6. Schematic of the GO structure [32].

In this work, GO was produced using a modified Hummers method [35]. The oxidation of graphite was realized using H_2SO_4+$NaNO_3$, and $KMnO_4$ at 5ºC. The solution was stirred overnight at 35ºC and then washed with HCl and water to neutralize the GO solution. Sonication process was apply during 2 hours to achieve exfoliation. The material has been provided by

Ana M. Benito and Wolfgang K. Maser, from the Department of Chemical Processes and Nanotechnology at Instituto de Carboquímica ICB-CSIC in Zaragoza.

The GO experiments were realized using supplied GO flakes in solution. We deposited a drop of this solution on a grid. After we observed the grid in the TEM microscope to determinate the position and the quality of flakes, we used the FIB FEI Helios 650, a dual-beam in the clean room of INA for sample preparation. In this equipment, we selected the best flake to do the measurements and we transferred it to the chip used for the in situ electrical TEM experiments. The transfer is realized in two processes. Firstly, we cut the GO flake with the ion beam and weld it onto the micro-needle with Pt to transport it to the chip and place it in the correct position. Secondly, we contacted the flake to the metal contact pads of the chip and in one case Pt was used to connect the flake to the chip and in the other case, a polymer glue (curable by the electron beam) was used, see Fig. 7.
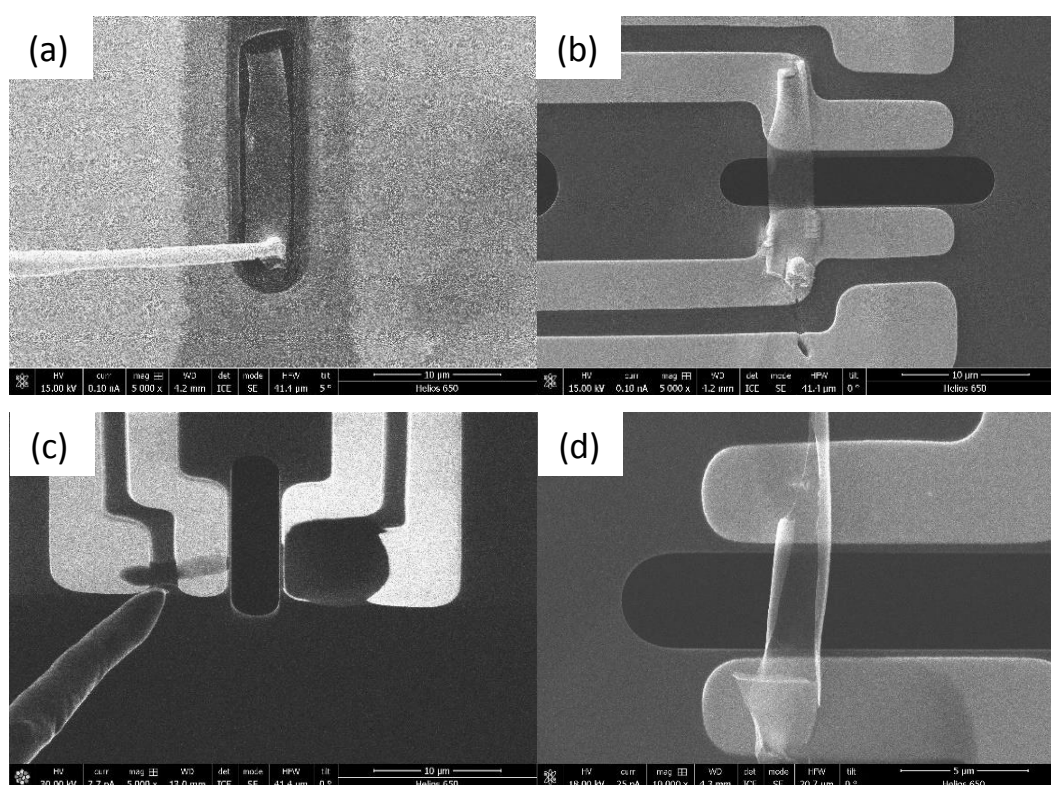

Figure 7. (a) Cutting of a GO flake, (b) Pt used to contact the flake with the nano-chip, (c) impregnation of the polymer glue on the nano-chip, (d) cured polymer glue used to contact the GO flake with nano-chip.

The holder with the nano-chip was introduced in the TEM microscope for developing the in situ electrical measurements. Depending the experiment that we carried out, we applied a voltage (flake with platinum) or a current,(flake with polymer) as we realized that we had a better control of the processes taking place by applying a current instead of a voltage.

Simultaneously, EEL spectra (in the low loss and core loss regions) were acquired for monitorizing the structural, chemical and property modifications during the measurements.

For the analysis and treatment of the EEL spectra, the integration quantification methods in core loss spectra were used to obtain the relative amount of each element contained in the sample. The elements contained in the GO were carbon, oxygen, nitrogen and calcium, of which the last two elements were considered as impurities. This quantification method permits us to estimate the relative amount of carbon atoms in the sample, as well as estimating the reduction rate of the GO.

In the case of carbon, the relative amount of carbon is taken and divided with respect to the sum of all elements, without taking into account the impurities. In the same way, it is possible to calculate the oxygen ratio in the sample.

$$\%C = \frac{[C]}{[C]+[O]} \qquad (2)$$

$$\%O = \frac{[O]}{[C]+[O]} \qquad (3)$$

For the thickness calculation, low loss EEL spectra were used. The log-ratio method was used in order to obtain the thickness of GO flake. This method is based on the Beer's absorption law:

$$\frac{t}{\lambda} = ln\frac{It}{I0} \qquad (4)$$

Where λ is the inelastic mean free path (IMFP) of the material, I_0 is the area under the Zero Loss Peak of the spectrum between -2 and 2 eV (ZLP), and I_t is the whole area under the spectrum up to 100 eV, as it is represented in figure 8.
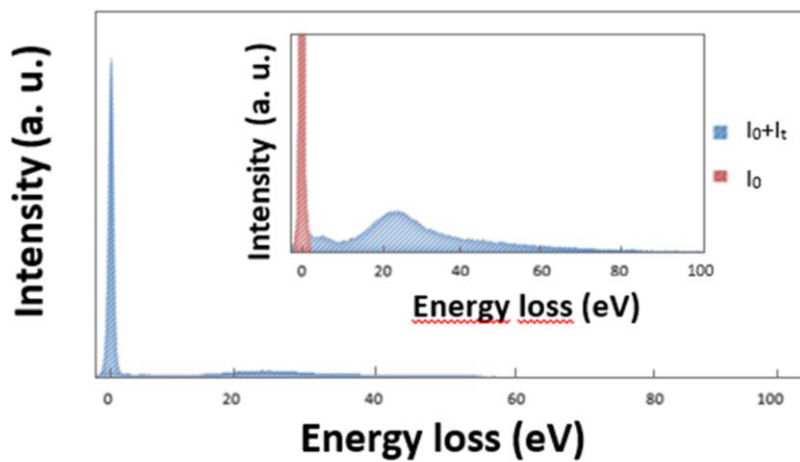

Figure 8. Low loss spectrum with the ratio of I_0 and I_t.

An accurate value of the thickness was obtained thanks to an accurate estimation of the IMFP value. To do that, it is necessary to take account the electron beam energy and collection semiangle of the measurements, important values in the next equation, which comes from [36,37]:

$$\lambda = \frac{106*F*E0}{Em*\ln(2\beta*\frac{E0}{Em})} \tag{5}$$

Where in this experiment E_0 is the electron beam energy with a value of 80 kV, β is the collection semiangle with a value of 19,7 mrad and E_m is the average energy loss, which can be approximated by $E_m = 7{,}6*Z_{\text{eff}}^{0,3}$

As we can appreciate by the value of E_m, it is important to take account of the effective atomic number value (Z_{eff}). This value was obtained by atomic concentration obtained in each element in the core loss spectrum, as shown the next equation:

$$Zef = \frac{\sum if iZi1,3}{\sum if iZi0,3} \tag{6}$$

Where f_i is the atomic fraction for each element i and Z_i is the atomic number for each element i.

Finally, sp^2 contain in GO samples was estimated for the different conductivity measurements realized. The estimation was realized using two different methods. One of them for spectra with low sp^2 quantity and the other one for spectra with high sp^2 quantity.

In the case of spectra with a low amount of sp^2 content, this method was based on a proportionality of the sp^2 fraction of a carbon material and the relative intensity of the π^* feature of its C-K edge. This translates into this equivalency between any two carbon materials (C and D, for example) taken from the literature [38,39,40]:

$$\frac{\frac{A_{\pi^*C}}{A_{\pi^*+\sigma^*C}}}{\%sp_C^2} = \frac{\frac{A_{\pi^*D}}{A_{\pi^*+\sigma^*D}}}{\%sp_D^2} \tag{7}$$

Where A_{π^*} is the area of the π^* feature, and $A_{\pi^*+\sigma^*}$ is the area of the $\pi^* + \sigma^*$ feature. For this analysis, it was necessary to calibrate and to deconvolute the core loss spectra using a Fourier ratio deconvolution, to account for the multiple scattering taking place. After that, a script was used to select a specific part of the spectrum between 280 and 310 eV. This spectral window contains the π* feature of the C-K edge of the spectrum and the σ* feature (in other words A π*+ σ*). This region is characteristic to study carbon [41,42].

The same process is used to select an area between 280 and 300 eV over the local energy loss minimum (around 290 eV) between $\pi*$ and $\sigma*$ peaks. In this second spectrum a fit is performed using 60 decreasing Gaussians method to represent $\pi*$ contribution including the decaying tail of the $\pi*$, placing it in 284 eV [42,43]. A Gaussian was also used at 294 eV to represent $\sigma*$ peak feature. This fit allows us to obtain the location, the width and the height of the $\pi*$ peak.
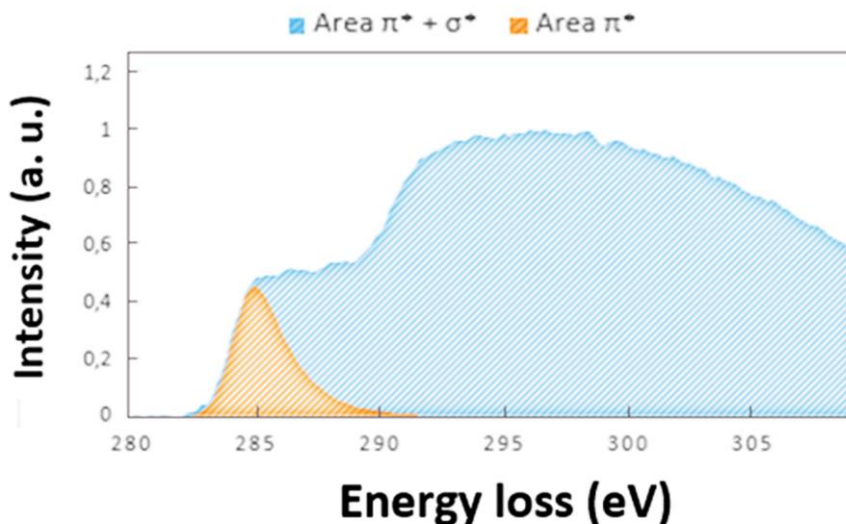

Figure 9. Core loss spectrum with the area ratio of the $\pi*$ and $\pi*+\sigma*$ peaks

Dividing the area of the sum of the 60 Gaussians in the fit ($A_{\pi*}$), which represent $\pi*$ peak, over the region of the spectrum with the $\pi*+\sigma*$ peaks, lets us obtain the value of y' which represent the relation of both areas [44]. For that goal, both spectral areas were integrated. For this, it was necessary to sum the area of each point in the spectrum multiplied by the energy step of the measurement, ΔE ($S_{\pi*+\sigma*}$ is multiplied by ΔE in the case of first spectrum and $S_{\pi*}$ multiply by ΔE in the case of second spectrum).

$$y' = \frac{A\pi*}{A\pi*+\sigma*} = \frac{S\pi* \times \Delta E}{S\pi*\sigma* \times \Delta E} = \frac{S\pi*}{S\pi*+\sigma*} \qquad (8)$$

In other words, the ratio of these areas equals the ratio of the total sum of these spectra over this spectral window. Finally, we can calculate % sp^2 using this equation:

$$\%sp^2 GO = \frac{y'_{GO}}{y'_{HOPG}} * \%sp^2 HOPG = \frac{y'_{GO}}{0,2} * 100 \qquad (9)$$

Where y'$_{GO}$ is the value calculated before, y'$_{HOPG}$ is 0,2 as referred to in the literature [40], and we assume a 100% of sp^2 in the highly oriented pyrolytic graphite (HOPG).

In the case of a high amount of sp^2 orbitals, the method explained before does not work due to orientation effects. For this reason, in these spectra we will use Multiple Linear Least Squares (MLLS) was used to determinate the quantity of sp^2 carbons in the GO. This method consists

in the use of two different spectra to estimate the quantity of sp^2 by means of the lineal combination of said spectra. In our case, a spectrum of a pure sample of sp^2 HOPG and the spectra of GO in the beginning of the experiment were used. We assume the HOPG again to have a 100% ratio of sp^2 contribution, and we can calculate the ratio of sp^2 at the beginning of the experiment using the method explained before.

For this, both spectra were normalized using a custom script. Moreover, the spectra were cut in the spectral window between 280 and 310 eV, the region where are π*+ σ* peaks. They were normalize using the following equation:

$$Snorm = \frac{S}{Sum(S)} \tag{10}$$

From there, a custom fit was applied using 8 Gaussians to both the initial spectra and the HOPG spectra, as shown in figure 10. Once these two spectra were adjusted, a custom script is used to cut the obtained spectra from different electrical measurements of GO. Spectra was cut by this script between 280 and 290 eV. This spectral window is where the π* peak is located.
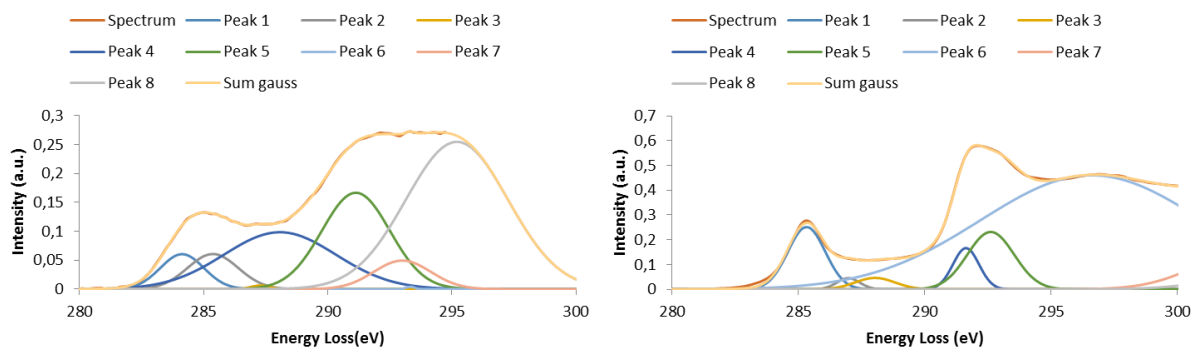

Figure 10. Representation of the Gaussian fit of the core loss spectra of the GO (left) and the HOPG (right) respectively.

Finally, a custom fitting function is created, where each spectrum is expressed as a linear combination of the two fitting spectra:

$$S = a * S_{GO} + b * S_{HOPG} = a * \sum G_{GO} + b * \sum G_{HOPG} \tag{11}$$

Where S is the spectra we are analyzing, a and b are the fitting coefficients, S$_{GO}$ and S$_{HOPG}$ are the Gaussian fits corresponding to the initial measurement and the pure HOPG respectively, and G$_{GO}$ are the individual Gaussians of GO and G$_{HOPG}$ are the Gaussians of HOPG. Once the adjustment gives us the values of a and b we use the following equation:

$$\%sp^2 = \frac{a*\%sp_{GO}^2 + b*\%sp_{HOPG}^2}{a+b} \tag{12}$$

It is assumed that $\%sp^2_{HOPG}$ is a 100% and with the calculation of $\%sp^2_{GO}$ with the method used before, it is possible to obtain the $\%sp^2$ of each one of the spectra with a high quantity of sp^2.

5 Results and discussion

5.1 In-situ TEM electron irradiation peapods

In this part of the work, we investigate the effect of the electron beam on the structure of peapods. For the experiments, four different grids were performed with a low quantity of contamination in our sample. Different areas of the sample were analyzed in order to determine a standard distribution of peapods, acquiring a variety of images before, during and after irradiating with the electron beam. During this irradiation functionalized fullerenes permit a change of the structure, generating new form hybrid of carbon nanomaterial called graphene nanoribbon (GNR) or closed edge of a carbon nanotube.

In the experiments (Figure 11), it is appreciated a process of $C_{59}N$-DT reactivity inside the nanotubes. We find that fullerenes close an open edge CNT and making an irradiation of fullerenes with the beam it is possible to close the edge. As Figure 11a shows, there is an open edge CNT. After irradiation with electron beam, it is appreciated the opening and the merging of fullerene with CNT until closed the structure. This process is possible due to energy applied with the beam. Theoretical researches are the best way to interpret and to understand these reactions between carbon nanostructures. For that, we based on "density functional based molecular dynamics simulations".

The process of fullerene merging with the nanotube wall and nanobud formation can be understood by the electron irradiation damage processes, and the subsequent formation and aggregation of intrinsic point defects as catalyzed by the beam. Under this situation, it is important to note that the probability of atom loss from a system is depend on the total knock-on cross section for a given atom. This depends on the strength of the local bonding, and in the case of 1D and 2D materials, the orientation of the layer with respect to the incoming electron beam [45]. From the chemical point of view, strong bound atoms in a pristine graphitic lattice are relatively difficult to remove, whereas weak bound atoms at defect sites are easier to remove. Now we will see the different elements and steps that we can consider for explaining the experimental results.
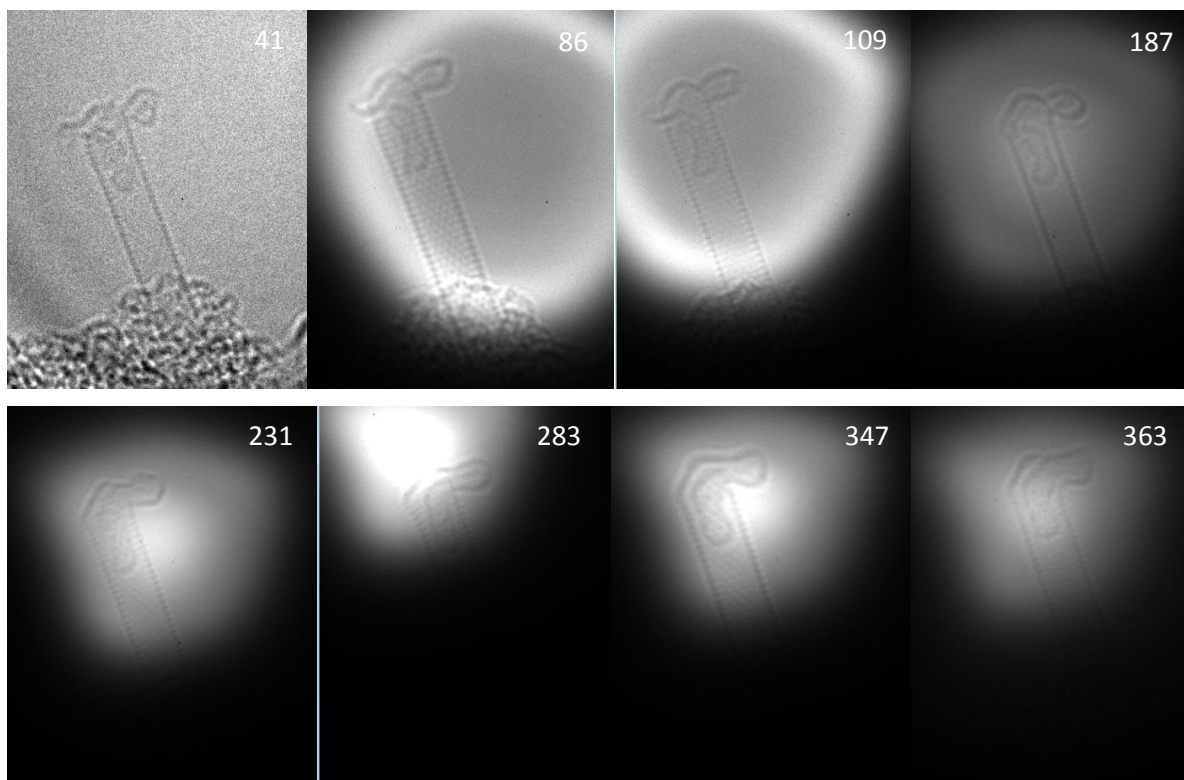
Figure 11. Eight-frames series sequence showing the evolution towards a nanobud formation via electron irradiation in a TEM.

The vacancy formation in single-walled carbon nanotubes has been theoretically investigated [45]. This shows that removal of a two-fold coordinated carbon neighbouring an existing vacancy has a maximum cross-section over an order of magnitude higher than removal of pristine carbon in a graphitic environment, 13.4 barns vs 1.4 barns. Subsequent atom removal, even though fully coordinated, still shows maximal cross-section of 5.2 barns, over four times that of atoms in the pristine lattice, due to the distorted local bonding. Extending this argument, given the lower inherent stability of atoms in fullerenes as compared to nanotubes, particularly irregular cages such as seen here, we expect much higher atom removal and rearrangement rates under the beam in the fullerene material than the tube. Equally, carbon in nanotube edges, containing necessarily pentagons and non-planar hexagonal lattice, will also be less stable and so more susceptible to beam damage than pristine nanotube side walls. In general, this implies that atom removal from pristine lattices will be difficult, but once the lattice is damaged, subsequent damage steps and increase of damaged areas will proceed much more rapidly.

As vacancy aggregation continues there will be a thermodynamic force to minimize the number of resultant carbon dangling bonds, with vacancy clusters showing particular stability such as V_2 where two vacancies are formed, and notably V_6 where a complete hexagonal carbon ring is removed from the lattice [46]. Theoretical modelling suggested a different, surprisingly stable form of V_6 is possible in bilayer material, where a hexagon of carbon atoms is removed, and the hexagon in the layer beneath rises up to lie midway between both layers, forming single

sp^3-C bonds with both the upper and lower sheet. In this way although the π-bonding of both sheets is disrupted, all the dangling σ-bonds in the system are saturated (Figure 12a). Subsequent irradiation will then remove these six carbon atoms.

More generally, vacancy loops in neighbouring sheets can stabilize the dangling bonds on neighbouring carbon atoms by cross-linking between the sheets [47]. This will result in "wormhole" or tunnel structures between neighbouring layers (Figure 12b), essentially small interlayer holes [48]. Additional irradiation will remove more material around the edge of these holes, expanding them further [49]. The result is a closed internal edge and a hole which expands with continued irradiation until eventually curvature is minimize and a nanobud structure is completed.
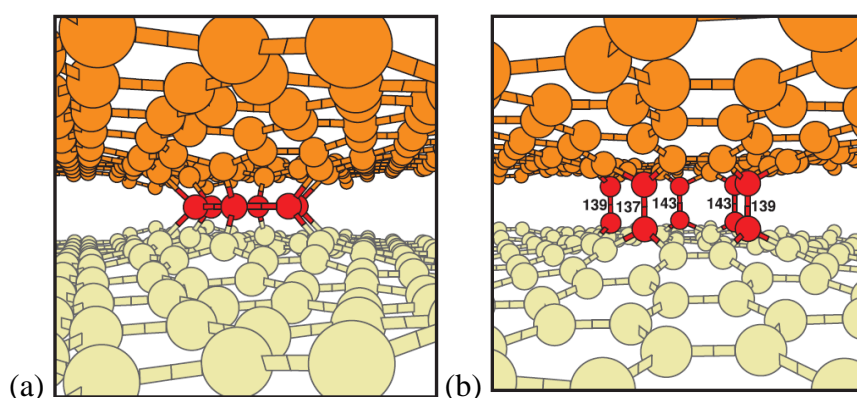

Figure 12. (a) The "mezzanine" V_6 defect structure showing interlayer sp^3 bonding, (b) the "wormhole" V_6 defect structure with three vacancies in each layer and cross-linking between undercoordinated carbon neighbours [46].

Starting from the initial fullerene configuration (Figure 11-86) we can indeed see more structural change in the internal and external fullerene cages as compared to the nanotube wall itself. The resolution difference of the side wall of nanotube below the fullerene cage (Figure 11-109) compared to the neighbouring wall suggests already there is a slightly lower density of carbon atoms in this vertical segment, consistent with formation of initial vacancy sites and mezzanine-type systems. This is still visible for several frames (130,133) before there is a sudden breakdown of material (187) consistent with the above model (initial atom removal from a mezzanine structure will be harder than the subsequent steps which would be expected to occur rapidly due to the higher knock-on cross-section in the partially complete structure). This results in a clear hole (231), which is confirmed by the presence of continuous material extending from the inside the nanotube into the fullerene structure (a chain barely visible in 231 but then clear in 283). This hole then expands through loss of edge material as described above (347, 351 and eventually 363), finishing in a continuous carbon nanobud surface.

This also allows the rapidly mutating internal fullerene structure to adapt to the new internal cavity shape and fill the relatively unstable nanobud. This secondary filling step is consistent with observations of irradiation in carbon peapods, where the fullerene breakdown results in internal nanotube formation, whose diameter depends on that of the external tube rather than the fullerenes, i.e. there is a clear templating effect of the external tube on the internal carbon reconstruction [50]. The current system (283-363) shows a more extreme version of the same effect where the internal extended fullerene structure adapts itself to closely match the unusual exterior nanotube-nanobud system.

5.2   In-situ electrical TEM graphene oxide measurements

In this work, we focused on the study of two different GO samples for the in situ TEM electrical measurements. One of them was contacted with Pt, using FIB deposition, to the nano-chip, and the other one was contacted with a polymeric glue cured by electron beam . Regarding the EELS analyses conducted in parallel with the electrical measurements, low-loss and core-loss EEL spectra were acquired for each applied power.

For carrying out these experiments, there are several risky, complicated and critical requirements & steps for the samples' preparation and the TEM measurements: (1) the GO flakes should be homogeneous and large enough (length>12 µm) for being able to fix them into the nano-chips ensuring a good contact; (2) these flakes should have an uniform thickness; (3) their thickness should be big enough (>35 nm) for being able to manipulate the flake, but not too big (<50-60 nm) for allowing reliable quantitative EELS analyses (multiple inelastic scattering effects limiting the quantification should be avoided [22]); (4) proper fixation of the flakes on the nano-chips for ensuring a good contact, avoiding/limiting any source of contamination that could have an impact on the measurements, see below; (5) carbon contamination from the TEM column or at the surface of the GO should be avoided as well as (6) any possibility of electron beam damage during the experiments (that is why, we worked at low voltage (80 kV) and under low dose conditions ($<1e^{-}/Å^2$)). For all these reasons, we have performed several attempts before getting the reliable results presented in the present manuscript.

Figures 13 (Figure 14) displays the C-K (O-K) edge extracted from different EEL spectra recorded in two different GO flakes. One of those flakes (left panel Fig. 13(14)) has been fixed to the nano-chip used for performing the in situ measurements via platinum FIB deposition. The second GO flake, EEL spectra displayed in the right panel of Fig. 13 (Fig. 14), has been glued to the nano-chip's electrical contacts using a polymer. For both flakes, their behavior (structure, chemistry and electrical properties) depending on the applied power is investigated.
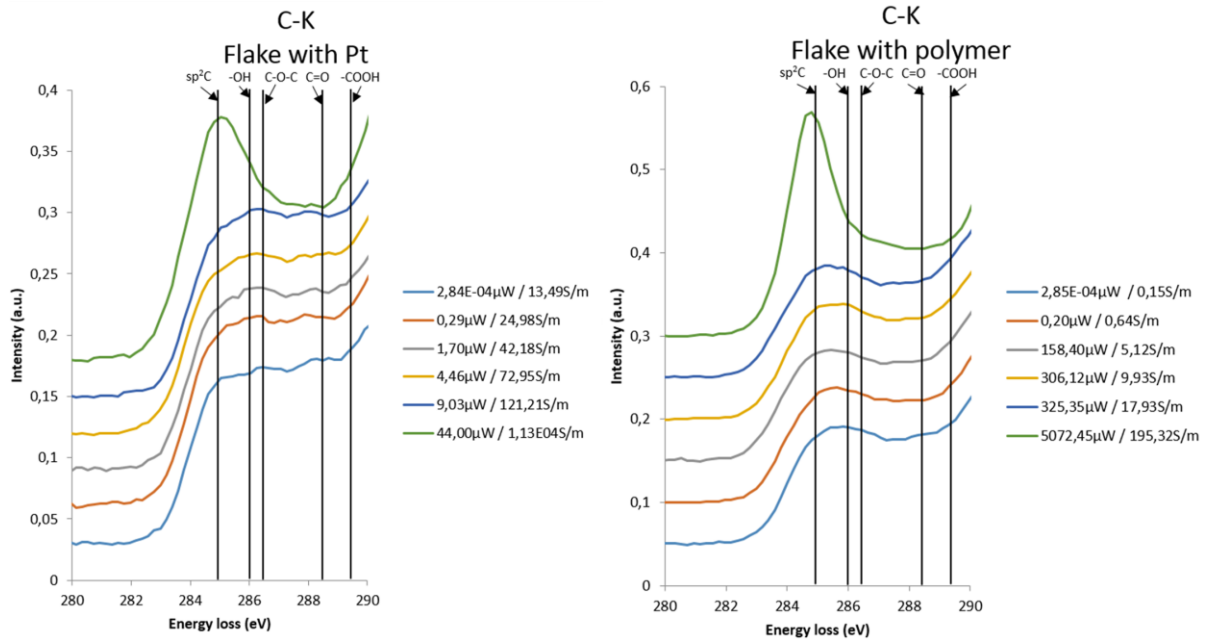
Figure 13. C-K edge of different EEL spectra recorded in: (left panel) a GO flake welded/contacted with Pt (FIB deposition) to the nano-chip used for performing the in situ electrical measurements; (right panel) another GO flake glued to the nano-chip's electrical contacts using a polymer. For both flakes, their behavior (structure, chemistry and electrical properties) within the applied power is investigated. The obtained conductivity values are also displayed in the graphs. The assignment and the identification of the different OFGs are marked in these spectra.

Figure 14. O-K edge for different EEL spectra recorded in: (left panel) a GO flake welded/contacted with Pt (FIB deposition) to the nano-chip used for performing the in situ electrical measurements; (right panel) another GO flake glued to the nano-chip's electrical contacts using a polymer. For both flakes, their behavior (structure, chemistry and electrical properties) within the applied power is investigated. The obtained conductivity values are also displayed in the graphs. The assignment and the identification of the different OFGs are marked in these spectra.
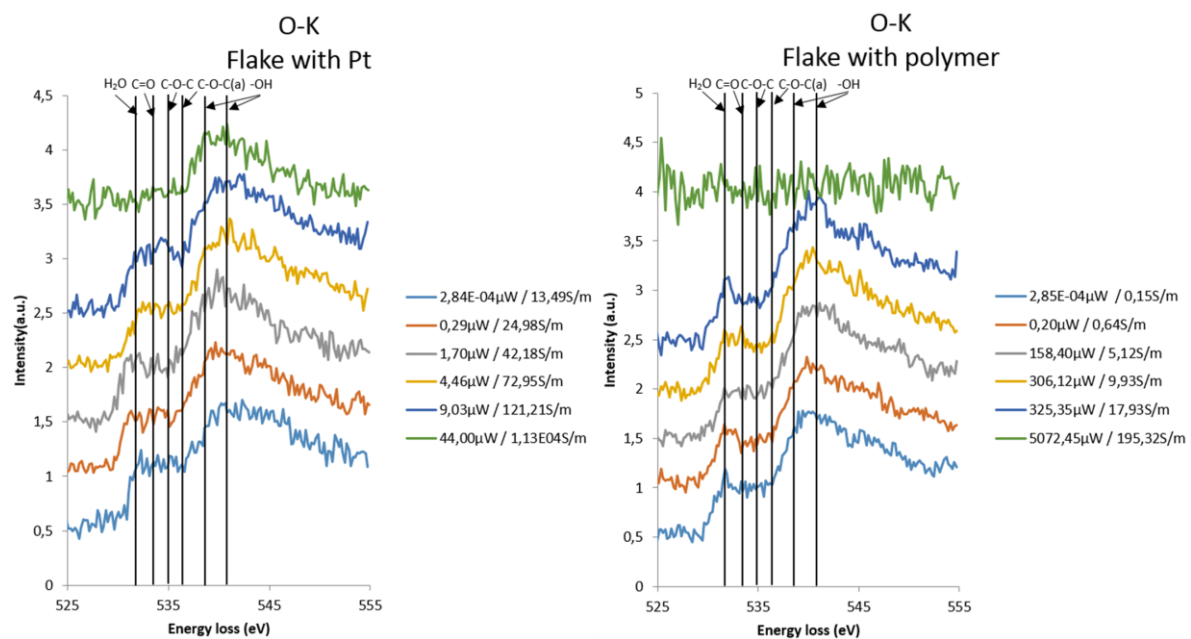
~ 21 ~

This has been achieved analyzing different aspects and parameters extracted from these EEL spectra.

One important aspect is to investigate the behavior of the GO functional groups during these measurements. These functional groups have been identified in the EEL spectra, peaks marked in the C-K and O-K edges (Fig. 13 and 14), based on different TGA and XPS studies [3,51,52]. As we will present below, these assignments help us to understand what and when the functional groups are desorbed from the GO structure. These are the different functional groups' assignments [53]:

1) The peak at 284.9 eV is this one associated to the signature pure sp^2 materials (graphitic atomic configuration C=C).

2) Hydroxyl group (-OH) can be found within the GO as physisorbed water (peak at 531.6 eV). Two peaks at 286 and 538.5 eV indicate that -OH groups can also be attached to the carbon structure.

3) Epoxide groups (C-O-C) can be identified due to the presence of the peaks at 286.6 eV (aromatic and non-aromatic), 534.9 eV non-aromatic and 536.2 eV aromatic.

4) The peaks at 288.4 eV and 533.6 eV correspond to the presence of carbonyl group (C = O).

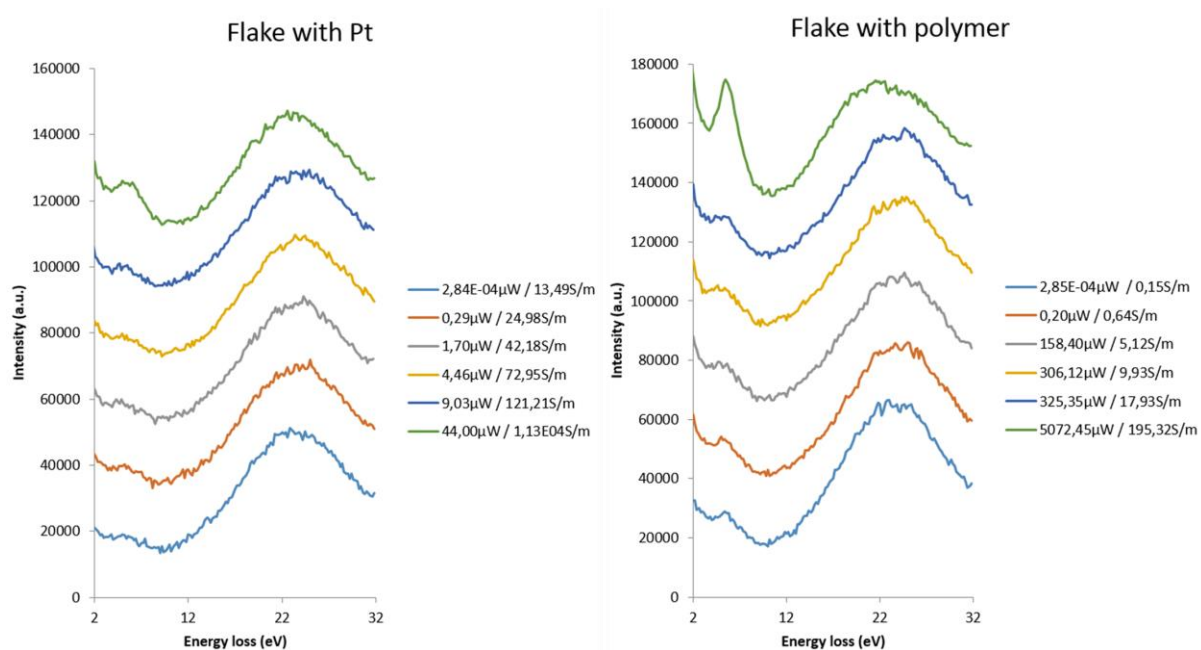5) Finally, the peak at 289.4 eV can be attributed to carboxyl group (-COOH) groups.

Figure 15. Plasmon region for different EEL spectra recorded in: (left) a GO flake contacted with Pt (FIB deposition) to the nano-chip used for performing the in situ electrical measurements; (right) another GO flake glued to the nano-chip's electrical contacts using a polymer. For both flakes, their behavior (structure, chemistry and electrical properties) within

the applied power is investigated. The obtained conductivity values are also displayed in the graphs.

Figure 15 displays a selection of low-loss spectra acquired on both samples at different applied power. These spectra show the presence (and evolution, see below) of the $\pi*$ plasmon at ~5.5 eV and this one of the bulk total plasmon ($\pi*$ and $\sigma*$) at ~25 eV. As described before, from the analysis of these spectra, we will get information about the thickness and the GO reduction and graphitization during the in situ TEM electrical measurements.
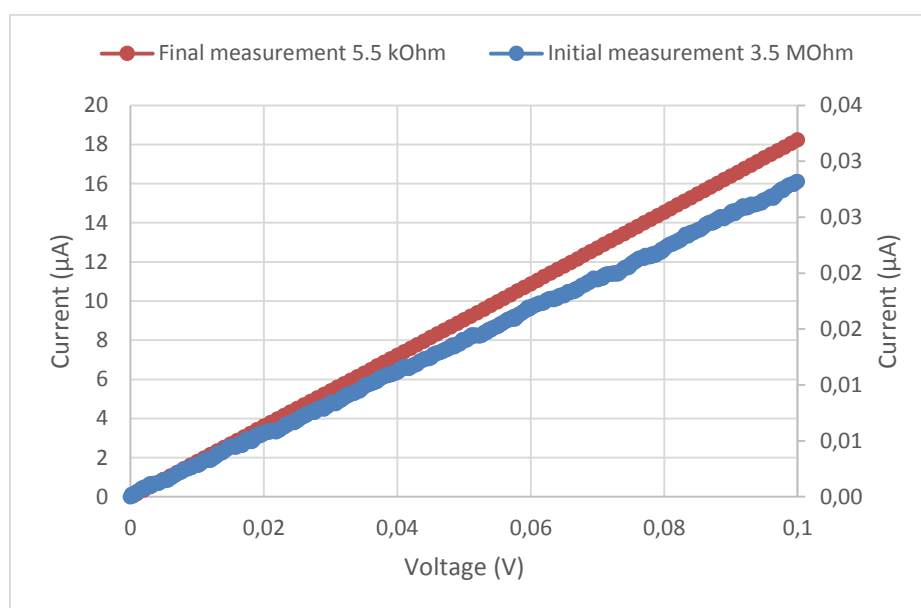

Figure 16. I-V characteristic of the GO flake welded/contacted with Pt (FIB deposition) to the nano-chip. The I-V curves have been acquired before and after GO reduction/transformation, see the text. Note the strongly different scale on the left and right y-axis.

Figure 16 shows two I-V characteristic curves for the GO sample flake contacted with Pt (FIB deposition) to the nano-chip for carrying out the measurements. These two I–V curves correspond to the initial measurement and once the transformation took place. It is worth mentioning that both curves exhibit ohmic behavior and then, as all the geometric parameters of the GO flakes are known from the TEM analyses, their conductivity can be obtained. These experiments also allow following the evolution of the conductivity and the GO's transformation (OFGs and water desorption -> its reduction and graphitization), see Fig. 17.
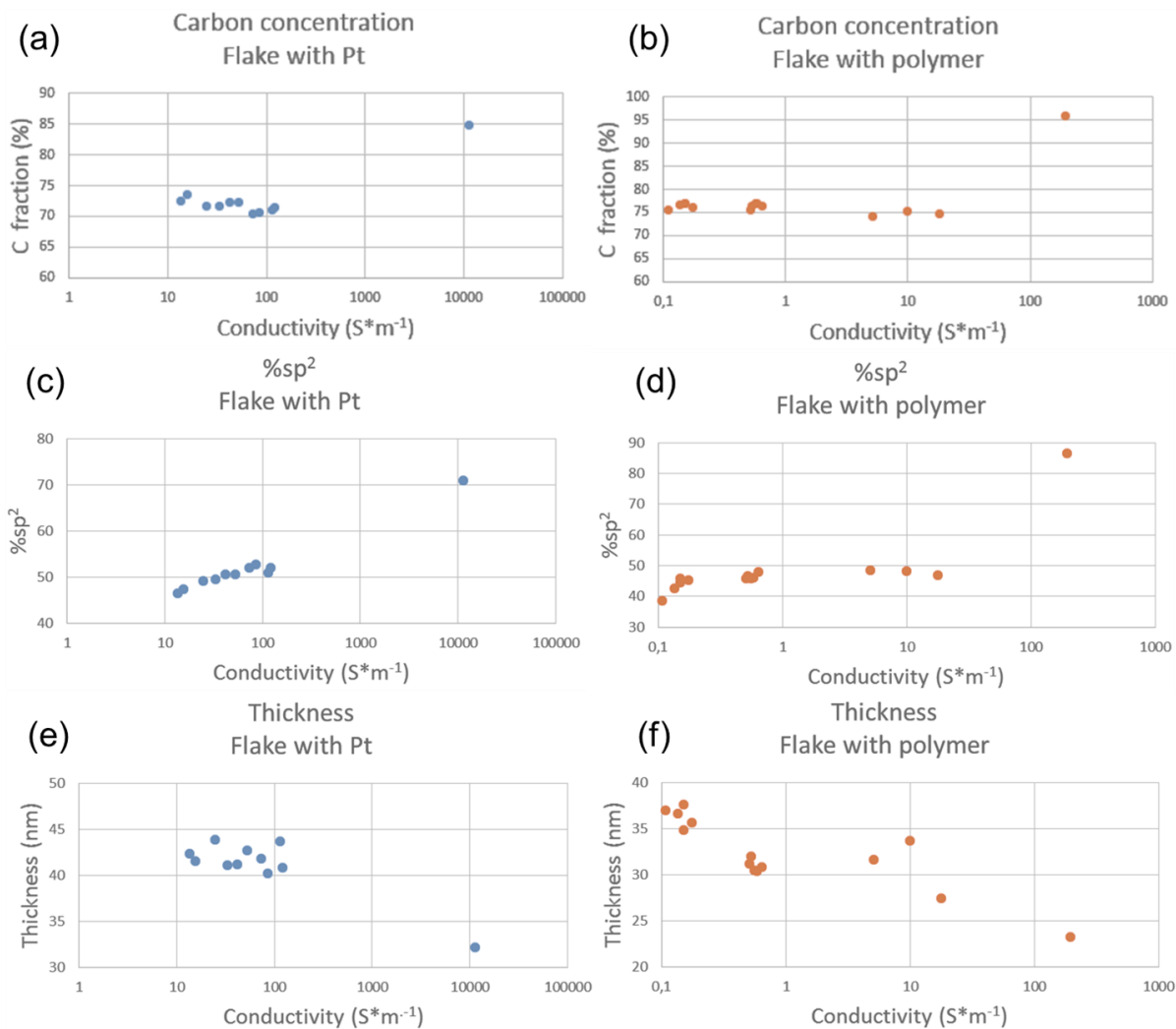
Figure 17. Different parameters (carbon fraction, sp^2 content and thickness) obtained from the EELS analyses developed on the two GO flakes and their evolution against their conductivity.

It is interesting to see the evolution of the GO material and, in particular, the functional groups during these in situ treatments for the two kind of samples (GO flake contacted using the Pt deposition and via the polymer). From all these measurements and analyses (see Figures 13-16 and Figure 17), we got the following information about the processes taking place, the materials and their transformation:

1) Due to the low conductivity values of the starting (original) GO flakes, a large power (sourcing voltage or current depending on the flake, see above) should be applied. In the case of the GO flake connected to the nano-chip using a polymer, the applied power is significantly higher (two orders of magnitude) than this one applied to the GO flake connected using Pt. This is due to the insulating character of the polymer and this also indicates that this contacting procedure is not very efficient/appropriated, see also point #2(c) below. This is also confirmed by the low starting conductivity values of the starting GO as well as by the low conductivity values reached at the end of the experiments.

2) We neglect any electron irradiation effect during the TEM analyses or at least, these could have a very limited impact on the measurements. Thus, the observed transformations on the GO flakes are electrically driven (Joule heating). Indeed, the GO flakes are resistively heated up and then, while the temperature is increasing, the conductivity is also increasing. We observed a progressive thermal reduction process of the graphene oxide for both of the flakes, even if their behavior during the treatments and the reached temperatures of both of them are different. Thus, we can analyze the changes of the three parameters (thickness, sp^2 ratio and C/O), which are related with the structural and chemical modifications:

(a) For the GO flake using the polymer for contacting the flake with the nano-chip, we can observe a thinning of almost 15% for the first four spectra and an increasing of ~10 % the sp^2 ratio. These effects can be attributed to the desorption of the physisorbed water and the desorption of some of the oxygenated functional groups (epoxide and carboxyls).

In the other case, GO flake connected using Pt, there is also a progressive increase of the conductivity, but for the first steps, there are no significant changes for the other parameters (t, sp^2% and C/O), indicating that only some physisorbed water is desorbed.

(b) For both flakes, at a certain point (the 5th EEL spectra/results), there is an increase of 18-25% of the sp^2 %. However, only in the case of the polymer glued flake another modification (a reduction of ~25% of the thickness) can be observed. We can then deduce that the reached temperature is not very high, below 500 ºC, and that under these conditions, only a partial desorption of the chemisorbed water and other functional groups as carbonyl ones from the edge of the flakes.

(c) Final step (6th EEL spectra in green): here both flakes suffer abrupt changes, restoring in both cases the sp^2 hybridization (recovering C=C bonds, graphitic structure). However, at some point, they are different, therefore we will describe them separately:

- Pt – GO flake: the conductivity reaches a value of 11350 S/m, which is three orders of magnitude higher than the starting value, and 4-6 times higher than this one found in the literature for other thermal reduction treatments [24]. At this point, some Pt nanoparticles (NPs) were observed on top of the flake. Their origin is likely the Pt-containing precursor molecules that adsorbed on the GO flake and surrounding contact areas during the connection of the flake using FIB-induced Pt deposition. Upon reaching a critical power, those molecules migrate on the surface and organic parts are removed leaving Pt-NPs behind. The high-obtained conductivity value can be related, at some point, to the presence of these Pt NPs. Indeed, even if we observe important

modifications of the three monitored parameters (thickness, sp^2 ratio and C/O), indicating a significant reduction and graphitization of the GO flake, this reduction and graphitization is not total. Thus, these modifications cannot justify *per se*, so high conductivity values.

In addition, the fact that [C] still ~85% and that the sp^2 ~72% suggest that the reached temperature is ~500C [53]. Thus, carbonyl groups and some extra chemisorbed water can be desorbed, but the hydroxyl groups still present in the flakes.

- Polymer – GO flake: in this case, the conductivity is two order the magnitude higher than this one at the beginning of the experiment, but the value ~195 S/m is very low if we compare with the literature for rGO materials with this low amount of oxygen (< 5%), which should be few thousand of S/m [24]. This is likely because the contacts are not good due to the presence of the polymer. This point has also a direct consequence into the GO's transformation, because due to this resistance, the Joule heating will be higher than in the other case, reaching temperatures higher than 1200C [53]. Indeed, this is why in this flake we measure C/O close to 97%, sp^2 content of ~87 % (60% increasing) and thinning of ~40%. These changes indicate a good reduction and graphitization of the GO, including the desorption of hydroxyl groups [53].

6 Conclusions and perspectives

The in-situ TEM analyses on these two carbon-based nanomaterials (peapods and GO) have illustrated the unique possibilities of this technique for transforming and studying the matter at the local (atomic scale).

For the endohedral functionalized SWNTs case, we were able to produce these hybrid systems. Thus, we filled SWCNTs with fullerenes for obtaining the peapods. In addition, we in situ investigated the evolution of these fullerenes under electron irradiation. We monitored the formation of a new nanostructure - a nanobud. We then proposed a plausible mechanism for the formation of such nanostructure. The high electron dose applied to one of these peapods makes possible that the energy absorbed by the fullerene at the surface of the nanotube provokes the generation of vacancies, which can facilitates the interaction with atoms of the nanotube wall for forming the nanobud.

In order to improve the knowledge of graphene oxide, we have developed in situ electrical TEM measurements combined with EELS analyses. We have investigated the relationship between

the conductivity values and the reduction and graphitization of the GO. We have identified and monitored the presence and the behavior of different oxygen functional groups forming the GO in parallel with these electrical measurements. We shed light on the different GO transformations with the increment of temperature due to Joule heating effects. Besides, the desorption of physisorbed and chemisorbed water during these measurements has also been investigated and the consequences of these effects within the GO have been discussed, in particular, the thinning of the GO flakes. These experiments have also evaluated the impact of potential artifacts on the conductivity measurements.

The future works on this area are very promising. Here we focused on the transformation and structural studies of the peapods, however it opens the door for studying the properties of the produced new nanostructures. In addition, it could also be interesting the study of other different, related hybrid nanostructures.

Regarding GO, it would be interesting to compare our reduction method with some thermal methods for obtaining rGO. In addition, due to the appealing electrical properties of rGO, in particular their tuning possibilities as a function of the oxygen content, it would be interesting to try to achieve it in a more controlled way.

7 References

[1] Arenal, R. (2005). *Synthèse de nanotubes de nitrure de bore:études de la structure et des propriétés (vibrationnelles et électroniques),* (Doctoral dissertation, *Université de Paris-Sud XI, Orsay).*

[2] Eda, G., & Chhowalla, M. (2010). Chemically derived graphene oxide: towards large-area thin-film electronics and optoelectronics. *Advanced materials*, *22*(22), 2392-2415.

[3] Robertson, J. (2002). Diamond-like amorphous carbon. *Materials Science and Engineering: R: Reports*, *37*(4-6), 129-281.

[4] Loh, K. P., Bao, Q., Eda, G., & Chhowalla, M. (2010). Graphene oxide as a chemically tunable platform for optical applications. *Nature chemistry*, *2*(12), 1015.

[5] Chen, D., Feng, H., & Li, J. (2012). Graphene oxide: preparation, functionalization, and electrochemical applications. *Chemical reviews*, *112*(11), 6027-6053.

[6] Borini, S., White, R., Wei, D., Astley, M., Haque, S., Spigone, E., ... & Ryhanen, T. (2013). Ultrafast graphene oxide humidity sensors. *ACS nano*, *7*(12), 11166-11173.

[7]Sun, Y., Fu, K., & Lin, Y. I. (2002). Functionalized carbon nanotubes. (2002). *Accounts of Chemical Research*, *35*(12), 1096–1104.

[8]Popov, V. N., Kliment, S., & Popov, V. N. (2016). *Carbon Nanotubes : Properties and Application Carbon nanotubes : properties and application*. *43*(December), 61–102.

[9]Yang, H., Wu, S., Duan, Y., Fu, X., & Wu, J. (2012). Surface modification of CNTs and enhanced photocatalytic activity of TiO 2 coated on hydrophilically modified CNTs. *Applied Surface Science*, *258*(7), 3012–3018.

[10] Sevilla, M., Yu, L., Zhao, L., Ania, C. O., & Titiricic, M. M. (2014). Surface modification of CNTs with N-doped carbon: An effective way of enhancing their performance in supercapacitors. *ACS Sustainable Chemistry and Engineering*, *2*(4), 1049–1055.

[11]Smith, B. W., & Luzzi, D. E. (2000). Formation mechanism of fullerene peapods and coaxial tubes: A path to large scale synthesis. *Chemical Physics Letters*, *321*(1–2), 169–174.

[12] Melchionna, M., & Prato, M. (2014). Functionalization of carbon nanotubes. *Nanocarbon-Inorganic Hybrids: Next Generation Composites for Sustainable Energy Applications*, *141*, 43–70.

[13] Khlobystov, A. N., Britz, D. A., & Briggs, G. A. D. (2005). Molecules in carbon nanotubes. *Accounts of Chemical Research*, *38*(12), 901–909.

[14]Sloan, J., Dunin-Borkowski, R. E., Hutchison, J. L., Coleman, K. S., Clifford Williams, V., Claridge, J. B., … Green, M. L. H. (2000). The size distribution, imaging and obstructing properties of C60 and higher fullerenes formed within arc-grown single walled carbon nanotubes. *Chemical Physics Letters*, *316*(3–4), 191–198.

[15] Mao, S., Pu, H., & Chen, J. (2012). Graphene oxide and its reduction: modeling and experimental progress. *Rsc Advances*, *2*(7), 2643-2662.

[16] Ganguly, A., Sharma, S., Papakonstantinou, P., & Hamilton, J. (2011). Probing the thermal deoxygenation of graphene oxide using high-resolution in situ X-ray-based spectroscopies. *The Journal of Physical Chemistry C*, *115*(34), 17009-17019.

[17] Tararan, A. (2016). *Spectroscopy in fragile 2D materials: from Graphene Oxide to single molecules at hexagonal Boron Nitride* (Doctoral dissertation, Paris Saclay).

[18] Ruska, E. (1987). The development of the electron microscope and of electron microscopy. *Reviews of modern physics*, *59*(3), 627.

[19] Deepak, F. L., Mayoral, A., & Arenal, R. (Eds.). (2015). *Advanced Transmission Electron Microscopy: Applications to Nanomaterials*. Springer.

[20] Wu, X., & Zeng, X. C. (2008). First-principles study of a carbon nanobud. *ACS Nano*, *2*(7), 1459–1465.

[21] Williams, D. B., & Carter, C. B. (1996). The transmission electron microscope. In *Transmission electron microscopy* (pp. 3-17). Springer, Boston, MA.

[22] Egerton, R. F. (2011). *Electron energy-loss spectroscopy in the electron microscope*. Springer Science & Business Media.

[23]Shearing, P. R., Golbert, J., Chater, R. J., & Brandon, N. P. (2009). 3D reconstruction of SOFC anodes using a focused ion beam lift-out technique. *Chemical Engineering Science*, *64*(17), 3928–3933.

[24] Gross, K., Barragán, J. P., Sangiao, S., De Teresa, J. M., Lajaunie, L., Arenal, R., ... & Prieto, P. (2016). Electrical conductivity of oxidized-graphenic nanoplatelets obtained from bamboo: effect of the oxygen content. *Nanotechnology*, *27*(36), 365708.

[25] Baughman, R. H., Zakhidov, A. A., & De Heer, W. A. (2002). Carbon nanotubes - The route toward applications. *Science*, *297*(5582), 787–792.

[26] Basu-Dutt, S., Minus, M. L., Jain, R., Nepal, D., & Kumar, S. (2012). Chemistry of carbon nanotubes for everyone. *Journal of Chemical Education*, *89*(2), 221–229

[27]Brodie, B. C. (1858). on the Atomic Weight of Graphit. *Royal Society of London*, *149*, 423–429

[28] Beheshtian, J., Peyghan, A. A., & Bagheri, Z. (2012). Theoretical investigation of C 60 fullerene functionalization with tetrazine. *Computational and Theoretical Chemistry*, *992*(2), 164–167.

[29] Scharff, P., Risch, K., Carta-Abelmann, L., Dmytruk, I. M., Bilyi, M. M., Golub, O. A., … Durov, S. S. (2004). Structure of C60 fullerene in water: Spectroscopic data. *Carbon*, *42*(5–6), 1203–1206.

[30] Hasan, T., Scardaci, V., Tan, P. H., Rozhin, A. G., Milne, W. I., & Ferrari, A. C. (2007). Stabilization and "debundling" of single-wall carbon nanotube dispersions in N-methyl-2-pyrrolidone (NMP) by polyvinylpyrrolidone (PVP). *Journal of Physical Chemistry C*, *111*(34), 12594–12602.

[31] Geng, H. Z., Lee, D. S., Kim, K. K., Han, G. H., Park, H. K., & Lee, Y. H. (2008). Absorption spectroscopy of surfactant-dispersed carbon nanotube film: Modulation of electronic structures. *Chemical Physics Letters*, *455*(4–6), 275–278.

[32]Lerf, A., He, H., Forster, M., & Klinowski, J. (1998). Structure of graphite oxide revisited. *Journal of Physical Chemistry B*, *102*(23), 4477–4482.

[33] Downs, R. T., & Hall-Wallace, M. (2003). The American Mineralogist crystal structure database. *American Mineralogist*, *88*(1), 247-250.

[34] Acik, M., Mattevi, C., Gong, C., Lee, G., Cho, K., Chhowalla, M., & Chabal, Y. J. (2010). The role of intercalated water in multilayered graphene oxide. *Acs Nano*, *4*(10), 5861-5868.

[35] Stankovich, S., Dikin, D. A., Piner, R. D., Kohlhaas, K. A., Kleinhammes, A., Jia, Y., ... & Ruoff, R. S. (2007). Synthesis of graphene-based nanosheets via chemical reduction of exfoliated graphite oxide. *carbon*, *45*(7), 1558-1565.

[36] Malis, T., Cheng, S. C., & Egerton, R. F. (1988). EELS log-ratio technique for specimen-thickness measurement in the TEM. *Microscopy Research and Technique*, *8*(2), 193-200.

[37] Zhang, H. R., Egerton, R. F., & Malac, M. (2012). Local thickness measurement through scattering contrast and electron energy-loss spectroscopy. *Micron*, *43*(1), 8-15.

[38] Ferrari, A. C., Libassi, A., Tanner, B. K., Stolojan, V., Yuan, J., Brown, L. M., ... & Robertson, J. (2000). Density, sp 3 fraction, and cross-sectional structure of amorphous carbon films determined by X-ray reflectivity and electron energy-loss spectroscopy. *Physical Review B*, *62*(16), 11089.

[39] Liu, A. C. Y., Arenal, R., Miller, D. J., Chen, X., Johnson, J. A., Eryilmaz, O. L., ... & Woodford, J. B. (2007). Structural order in near-frictionless hydrogenated diamondlike carbon films probed at three length scales via transmission electron microscopy. *Physical Review B*, *75*(20), 205402.

[40] Berger, S. D., McKenzie, D. R., & Martin, P. J. (1988). EELS analysis of vacuum arc-deposited diamond-like films. *Philosophical Magazine Letters*, *57*(6), 285-290.

[41] Mkhoyan, K. A., Contryman, A. W., Silcox, J., Stewart, D. A., Eda, G., Mattevi, C., ... & Chhowalla, M. (2009). Atomic and electronic structure of graphene-oxide. *Nano letters*, *9*(3), 1058-1063.

[42] Tararan, A., Zobelli, A., Benito, A. M., Maser, W. K., & Stéphan, O. (2016). Revisiting graphene oxide chemistry via spatially-resolved electron energy loss spectroscopy. *Chemistry of Materials*, *28*(11), 3741-3748.

[43] D'Angelo, D., Bongiorno, C., Amato, M., Deretzis, I., La Magna, A., Compagnini, G., ... & Scalese, S. (2015). Electron energy-loss spectra of graphene oxide for the determination of oxygen functionalities. *Carbon*, *93*, 1034-1041.

[44] Lajaunie, L., Pardanaud, C., Martin, C., Puech, P., Hu, C., Biggs, M. J., & Arenal, R. (2017). Advanced spectroscopic analyses on a: CH materials: Revisiting the EELS characterization and its coupling with multi-wavelength Raman spectroscopy. *Carbon*, *112*, 149-161.

[45] Zobelli, A., Gloter, A., Ewels, C. P., & Colliex, C. (2008). Shaping single walled nanotubes with an electron beam. *Physical Review B - Condensed Matter and Materials Physics*, *77*(4), 1–8.

[46] Vuong, A., Trevethan, T., Latham, C. D., Ewels, C. P., Erbahar, D., Briddon, P. R., Heggie, M. I. (2017). Interlayer vacancy defects in AA-stacked bilayer graphene: Density functional theory predictions. *Journal of Physics Condensed Matter*, *29*(15).

[47] Telling, R. H., Ewels, C. P., El-Barbary, A. A., & Heggie, M. I. (2003). Wigner defects bridge the graphite gap. *Nature Materials*, *2*(5), 333–337.

[48] Kvashnin, D. G., Vancsó, P., Antipina, L. Y., Márk, G. I., Biró, L. P., Sorokin, P. B., & Chernozatonskii, L. A. (2015). Bilayered semiconductor graphene nanostructures with periodically arranged hexagonal holes. *Nano Research*, *8*(4), 1250–1258.

[49] Huang, J. Y., Qi, L., Li, J., Ding, F., Yakobson, B. I., & Lu, P. (2009). In-situ observation of graphene sublimation and edge reconstructions. *Microscopy and Microanalysis*, *15*(SUPPL. 2), 1164–1165.

[50] Abe, M., Kataura, H., Kira, H., Kodama, T., Suzuki, S., Achiba, Y., Maniwa, Y. (2003). Structural transformation from single-wall to double-wall carbon nanotube bundles. *Physical Review B - Condensed Matter and Materials Physics*, *68*(4), 5–8.

[51] Yang, D., Velamakanni, A., Bozoklu, G., Park, S., Stoller, M., Piner, R. D., ... & Ruoff, R. S. (2009). Chemical analysis of graphene oxide films after heat and chemical treatments by X-ray photoelectron and Micro-Raman spectroscopy. *Carbon*, *47*(1), 145-152

[52] Haubner, K., Murawski, J., Olk, P., Eng, L. M., Ziegler, C., Adolphi, B., & Jaehne, E. (2010). The route to functional graphene oxide. *ChemPhysChem*, *11*(10), 2131-2139.

[53] M. Pelaez-Fernandez, A. Bermejo-Solis, A.M. Benito, W.K. Maser and R. Arenal, *to be submitted.*